# Transdimensional surface wave inversion of the near surface
## Application to distributed acoustic sensing data

Dalkhani, Amin Rahimi; Hasani, Musab Al; Drijkoningen, Guy; Weemstra, Cornelis

**DOI**
10.1190/GEO2024-0151.1

**Publication date**
2025

**Document Version**
Final published version

**Published in**
Geophysics

**Citation (APA)**
Dalkhani, A. R., Hasani, M. A., Drijkoningen, G., & Weemstra, C. (2025). Transdimensional surface wave inversion of the near surface: Application to distributed acoustic sensing data. *Geophysics*, *90*(5), KS125-KS139. https://doi.org/10.1190/GEO2024-0151.1

GEOPHYSICS, VOL. 90, NO. 5 (SEPTEMBER-OCTOBER 2025); P. KS125–KS139, 13 FIGS.
10.1190/GEO2024-0151.1





# Transdimensional surface wave inversion of the near surface: Application to distributed acoustic sensing data

Amin Rahimi Dalkhani[1], Musab Al Hasani[2], Guy Drijkoningen[1], and Cornelis Weemstra[3]

## ABSTRACT

Distributed acoustic sensing (DAS) is a novel technology, which allows the seismic wavefield to be sampled densely in space and time. This makes it an ideal tool for retrieving surface waves, which are predominantly sensitive to the S-wave velocity structure of the subsurface. In this study, we evaluate the potential of DAS to image the near surface (top 50 m) using active-source surface waves recorded with straight fibers on a field in the province of Groningen, the Netherlands. Importantly, DAS is used here in conjunction with a Bayesian transdimensional inversion approach, making this the first application of such an algorithm to DAS-acquired strain-rate wavefields. First, we extract laterally varying surface wave phase velocities (i.e., "local" dispersion curves [DCs]) from the fundamental mode surface waves. Then, instead of inverting each local DC separately, we use a novel 2D transdimensional algorithm to estimate the subsurface's S-wave velocity structure. We develop a few modifications to improve the performance of the 2D transdimensional approach. Specifically, we develop a new birth-and-death scheme for perturbing the dimension of the model space to improve the acceptance probability. In addition, we use a Gibbs sampler to infer the noise hyperparameters more rapidly. Finally, we introduce local prior information (e.g., S-wave logs) as a constraint to the inversion, which helps the algorithm to converge faster. We first validate our approach by successfully recovering the S-wave velocity in a synthetic experiment. Then, we apply the algorithm to the field DAS data, resulting in a smooth laterally varying S-wave velocity model. The posterior mean and uncertainty profiles identify a distinct layer interface at approximately 20 m depth with a sharp increase in velocity and uncertainty at that depth, aligning with borehole log data that indicate a similar velocity increase at the same depth.

## INTRODUCTION

After initial distributed acoustic sensing (DAS) field trials (Paulsson et al., 1997; Bostick, 2000; Johannessen et al., 2012; Molenaar et al., 2012), the DAS technique has been investigated and applied in the context of a variety of geophysical problems (e.g., Daley et al., 2013; Lindsey et al., 2017; Barone et al., 2021; Mata Flores et al., 2023). Due to the dense sampling of the wavefield and its broadband character, DAS also has become popular to sample surface waves in active (e.g., Qu et al., 2023; Yust et al., 2023) and passive (e.g., Ajo-Franklin et al., 2019; Nayak et al., 2021) surveys. Surface waves are useful because of their wave speed's sensitivity to the subsurface's S-wave velocity.

A material's S-wave velocity is, to a large extent, determined by its shear strength (or stiffness). Consequently, the S-wave velocity of the near surface is a valuable parameter in many subsurface engineering applications. Because the velocity of surface waves strongly depends on that S-wave velocity, near-surface S-wave velocity models are frequently derived from surface wave measurements (Socco et al., 2010). Typically, two types of surface waves are recorded: Rayleigh and Love waves (Aki and Richards, 2002). Surface waves are dispersive when the S-wave velocity varies as a function of depth, meaning that different frequencies propagate with different velocities. A surface wave's propagation velocity at an individual frequency is referred to as that frequency's phase velocity. The first step in surface wave imaging is usually the retrieval of

Manuscript received by the Editor 4 March 2024; revised manuscript received 3 March 2025; published ahead of production 19 May 2025; published online 7 August 2025.
[1]Delft University of Technology, Department of Geoscience and Engineering, Delft, The Netherlands. E-mail: a.rahimidalkhani@tudelft.nl (corresponding author); g.g.drijkoningen@tudelft.nl.
[2]Petroleum Development Oman, Muscat, Oman. E-mail: musab.alhasani@hotmail.com.
[3]Delft University of Technology, Department of Geoscience and Engineering, Delft, The Netherlands and Royal Netherlands Meteorological Institute, Seismology and Acoustics, Delft, The Netherlands. E-mail: kees.weemstra@knmi.nl.

the frequency-dependent phase velocities. An inversion subsequently results in a model of the S-wave velocity as a function of depth (Schaefer et al., 2011; Zhang et al., 2020).

Conventionally, in an active-source surface wave analysis, a dispersion curve (DC) is retrieved from each common-shot record using multichannel analysis of surface waves (Park et al., 1999), assuming that the subsurface is a stack of horizontal layers. Then, an inversion algorithm is used to recover a 1D S-wave velocity profile (e.g., Vantassel et al., 2022; Qu et al., 2023). Due to the dense spatial sampling and the high-frequency content of active-source DAS surveys, however, the lateral resolution could in principle be increased significantly (Barone et al., 2021). Consequently, to account for the lateral variation in the subsurface's velocity structure, many authors suggest recovering local DCs (e.g., Neducza, 2007; Luo et al., 2008; Vignoli et al., 2011; Barone et al., 2021). These local DCs then can be used in an inversion algorithm to recover a 2D profile (or 3D cube) of the subsurface S-wave velocity (Vignoli et al., 2016; Barone et al., 2021).

Several approaches have been proposed to recover lateral variations in the subsurface's S-wave velocity, most of them based on laterally varying DCs. The most common approach involves the application of a moving window to the recorded shot gathers in the time-space domain (e.g., Bohlen et al., 2004; Luo et al., 2008; Socco et al., 2009; Boiero and Socco, 2010). The windowed part of the data is then transformed into a spectral domain to estimate the local DC at the location of the center of that window. Alternatively, multioffset phase analysis (MOPA) (Vignoli et al., 2016) can be used to recover lateral variations (Barone et al., 2021). Vignoli et al. (2016) and Barone et al. (2021) successfully retrieve laterally varying fundamental mode DCs using MOPA.

In the presence of lateral variations, the dispersion relation varies as a function of location. In that case, the different DCs are often inverted independently using a 1D inversion algorithm (e.g., Bohlen et al., 2004; Socco et al., 2009; Vignoli et al., 2016; Barone et al., 2021), after which the independently inverted 1D profiles are pieced together to obtain a 2D (or 3D) S-wave velocity pseudosection (or pseudocube). However, by independently inverting the adjacent DCs, lateral correlations in the subsurface structure are ignored (Zhang et al., 2020). Socco et al. (2009) propose to invert all DCs simultaneously to mitigate the solution's nonuniqueness and retain lateral smoothness. They use a laterally constrained least-squares algorithm in which each 1D model is linked to its neighbors. In this study, we invert all the DCs simultaneously using a 2D transdimensional algorithm (Bodin and Sambridge, 2009). As such, we retain lateral correlations of the S-wave velocity and circumvent (rather arbitrary) smoothing and damping procedures (e.g., Xia et al., 1999).

In this study, we apply the MOPA algorithm to surface waves extracted from a 2D active-source DAS survey. The DAS data are recorded in the province of Groningen in the north of the Netherlands using straight and helically wound fibers (for more details, see Hasani and Drijkoningen [2023]). However, we use the straight fibers in this study to retrieve surface wave phase velocities. As such, we recover the laterally varying fundamental mode local phase velocities. Importantly, we then invert all the DCs simultaneously using the nonlinear 2D transdimensional tomographic algorithm (Bodin and Sambridge, 2009). This transdimensional inversion algorithm has been originally developed for surface wave traveltime tomography. Subsequently, it has been applied to many geophysical problems (e.g., Dettmer et al., 2012; Ghalenoei et al., 2022; Yao et al., 2023; Rahimi Dalkhani et al., 2024).

We modify and adapt the transdimensional algorithm for better application to DAS data by refining the birth/death proposal scheme to improve the acceptance ratio and sampling efficiency. In addition, we propose and implement a simple efficient method to handle unknown data uncertainty (i.e., noise level). Finally, we introduce a technique to incorporate borehole data as prior information to constrain the inversion. These allow us to generate a 2D S-wave velocity image (vertical cross section) of the subsurface with improved lateral correlation. We validate the obtained 2D S-wave velocity section using S-wave velocity logs obtained from two boreholes located at two specific points on the acquisition line.

## THEORY AND METHODOLOGY

In this section, we detail the various methods used in this study. First, we describe how the surface waves are extracted from the fiber-optic recordings. Subsequently, we explain how we locally estimate the surface waves' phase velocity as a function of frequency. Finally, we provide the details of the implementation of the Markov chain Monte Carlo (MCMC). Figure 1 shows the detailed flowchart of the proposed algorithm.

### Phase velocity retrieval

In case the subsurface is laterally invariant, the relation between phase ($\phi$) and offset ($x$) will be linear at each discrete frequency ($f_i$), with the slope coinciding with the wavenumber ($k$). This can be formulated as (Strobbia and Foti, 2006)

$$\phi(f_i, x) = k(f_i)x + \phi_0(f_i), \tag{1}$$

where $\phi_0$ is the phase at the location of the source. Equation 1 allows the estimation of a wavenumber by means of a least-squares fit of the phase-offset data at each discrete frequency $f_i$, i.e., using a linear regression (for detailed formulation, see Strobbia and Foti [2006]). The estimated wavenumber ($k(f_i)$) can be translated to the frequency-dependent phase velocity ($\mathrm{c}_p(f_i)$) using

$$\mathrm{c}_p(f_i) = \frac{2\pi f_i}{k(f_i)}, \tag{2}$$

where $i = 1, 2, \ldots, N_f$ and $N_f$ denotes the number of discrete frequencies. This approach is referred to as MOPA (Strobbia and Foti, 2006; Vignoli and Cassiani, 2010).

In the presence of (smooth) lateral variations, equation 1 can be formulated such that the wavenumber $k$ varies as a function of offset and frequency. That is, $k = k(f_i, x^{(c)})$, where $x^{(c)}$ denotes the center position of a set of adjacent (Fourier-transformed) wavefield recordings running from $x^{(c)} - W/2$ to $x^{(c)} + W/2$ (here, $W$ is the spatial window along which $k(f_i, x^{(c)})$ is assumed to be constant). Vignoli et al. (2011) "move" this spatial window along the recording line with small steps (i.e., significantly smaller than $W$). This is done separately for each discrete frequency, allowing $W$ to be frequency dependent (Vignoli et al., 2016). The wavenumbers are subsequently derived using linear regression according to equation 1. These laterally varying wavenumbers are then converted to laterally varying phase velocities $\mathrm{c}_p(f_i, x^{(c)})$ using equation 2. Snice the lateral resolution of the surface waves is directly related to the wavelength (Barone et al.,

DOI:10.1190/geo2024-0151.1

2021), Vignoli et al. (2016) propose to have the spatial window length $W$ be a function of the wavelength of the surface waves.

In this study, we use the MOPA algorithm of Vignoli et al. (2016) to estimate local DCs. Chiefly, this is because of the algorithm's robustness and simplicity. However, a drawback of the MOPA algorithm is that it can only be applied to a single surface wave mode. Therefore, only one mode will be considered, and other (potential) surface wave modes will be muted. Finally, it should be understood that the recovered wavenumbers are associated with the wavefield. That is, they will deviate from the medium's true wavenumber distribution (sometimes referred to as "structural wavenumbers") (Wielandt, 1993), with the discrepancy between the two being larger for more heterogeneous subsurfaces.

## Transdimensional surface wave inversion

The 2D transdimensional tomographic algorithm by Bodin and Sambridge (2009) is developed for surface wave traveltime tomography (for individual discrete frequencies). Here, we modify the algorithm to invert all DAS-derived DCs simultaneously. Our transdimensional algorithm uses a 2D Voronoi tessellation to parameterize the subsurface, in combination with a reversible jump MCMC (RJMCMC). A single unique model is defined by the number of Voronoi cells, their nuclei, and the S-wave velocity assigned to them. Note that the location of an individual Voronoi cell is defined by the location of its nucleus and that its geometry is controlled by its neighboring cells. As such, it allows a variable parameterization of the subsurface, meaning that the number of Voronoi cells, their locations, and the assigned velocities are all unknowns (Rahimi Dalkhani et al., 2021). Because the number of variables is a variable itself, this algorithm is referred to as transdimensional (Bodin and Sambridge, 2009). The transdimensional parameterization allows the algorithm to sample the posterior, without the need to introduce any kind of regularization (Bodin and Sambridge, 2009). Effectively, the regularization is inherent in the algorithm.

The transdimensional algorithm is a Bayesian inference method that aims to sample the posterior probability density (henceforth "posterior") of the model parameters $\mathbf{m}$, given the observed data $\mathbf{d}$. The posterior $p(\mathbf{m}|\mathbf{d})$ is proportional to the product of the likelihood $p(\mathbf{d}|\mathbf{m})$ and the prior $p(\mathbf{m})$ (Tarantola, 2005; Bodin and Sambridge, 2009):

$$p(\mathbf{m}|\mathbf{d}) \propto p(\mathbf{d}|\mathbf{m})p(\mathbf{m}). \tag{3}$$

The prior probability distribution $p(\mathbf{m})$ incorporates all (a priori) known independent information about the model space. Similar to Bodin and Sambridge (2009), we consider an (uninformative) uniform prior for all model parameters.

The likelihood function $p(\mathbf{d}|\mathbf{m})$ plays a fundamental role in the inference of the model space as it quantifies the probability of the observed laterally varying DCs given a specific velocity model. Assuming the likelihood to be Gaussian, it is formulated as

$$p(\mathbf{d}|\mathbf{m}) = A \exp\left(-\frac{\phi(\mathbf{m})}{2}\right), \tag{4}$$

where $A$ is a normalization factor and $\phi(\mathbf{m})$ is a simple least-squares misfit ($\phi(\mathbf{m}) = \|((\mathbf{g}(\mathbf{m}) - \mathbf{d})/\sigma)\|^2$). The vector $\mathbf{m}$ contains the parameters describing the proposed model. Due to the variable number of Voronoi cells, its length (or its "dimension") changes while the posterior is being sampled. Furthermore, $\mathbf{g}$ is the modeled laterally varying phase velocity and $\sigma$ represents the data uncertainty for the phase velocity at different discrete frequencies and locations.

It is worth noting that the input data in our case (i.e., laterally varying, frequency-dependent phase velocities along a 2D line) are different from the traveltimes used in Bodin and Sambridge (2009). Consequently, a different forward function is necessary to compute the modeled data. For this purpose, we use a MATLAB package developed by Wu et al. (2019) using the reduced delta matrix method proposed by Buchen and Ben-Hador (1996). This algorithm computes the DC (i.e., phase velocity versus frequency) in a 1D earth model. Therefore, to model the laterally varying DCs, we take the 1D velocity profile at each location and compute the DCs independently. However, it should be understood that these DCs are not uncorrelated: the correlation between "adjacent" DCs results from the Voronoi partitioning.

### *Reversible jump MCMC*

The RJMCMC draws samples from the posterior distribution using a Metropolis-Hasting (MH) algorithm, which includes changing the dimension of the model space. The process starts with some random initial model $\mathbf{m}$, as shown in Figure 1. Then, the algorithm draws the next sample of the chain by proposing a new model $\mathbf{m}'$ based on a known proposal probability function $q(\mathbf{m}'|\mathbf{m})$, which only depends on the current state of the model $\mathbf{m}$. The proposed model $\mathbf{m}'$ will be accepted with probability (Bodin and Sambridge, 2009):

$$\alpha(\mathbf{m}'|\mathbf{m}) = \min\left[1, \frac{p(\mathbf{m}')}{p(\mathbf{m})}\frac{p(\mathbf{d}|\mathbf{m}')}{p(\mathbf{d}|\mathbf{m})}\frac{q(\mathbf{m}|\mathbf{m}')}{q(\mathbf{m}'|\mathbf{m})} \times |\mathbf{J}|\right], \tag{5}$$

where $p(\mathbf{m}')/p(\mathbf{m})$ is the prior ratio, $p(\mathbf{d}|\mathbf{m}')/p(\mathbf{d}|\mathbf{m})$ is the likelihood ratio, $q(\mathbf{m}|\mathbf{m}')/q(\mathbf{m}'|\mathbf{m})$ is the proposal ratio, and $\mathbf{J}$ is the Jacobian associated with the transformation from $\mathbf{m}$ to $\mathbf{m}'$. The latter is needed to account for scale changes involved when the perturbation involves a jump between dimensions (Green, 1995).

The acceptance probability $\alpha(\mathbf{m}'|\mathbf{m})$ is the key to ensure that the samples will be generated according to the target posterior distribution $p(\mathbf{m}|\mathbf{d})$. Similar to Bodin and Sambridge (2009), we use four perturbation types to propose a new model ($\mathbf{m}'$) based on the current model ($\mathbf{m}$). These are nuclei *move*, velocity *update*, *birth*, and *death* steps. We parameterize the subsurface using the aforementioned (2D) Voronoi tesselation. As derived in Bodin and Sambridge (2009), the acceptance probability in the case of a move or update step (i.e., no change in model dimension) reads

$$\alpha(\mathbf{m}'|\mathbf{m}) = \min\left[1, \exp\left(\frac{\phi(\mathbf{m}) - \phi(\mathbf{m}')}{2}\right)\right]. \tag{6}$$

Note that this acceptance probability only depends on the likelihood ratio because (1) the priors for $\mathbf{m}$ and $\mathbf{m}'$ coincide for models of the same dimension and (2) the proposal distribution is symmetrical if the dimension of the model space stays the same (i.e., $q(\mathbf{m}'|\mathbf{m}) = q(\mathbf{m}|\mathbf{m}')$; Bodin and Sambridge, 2009).

For a birth step, Bodin and Sambridge (2009) propose to randomly select a point from an underlying finite (and dense) 2D grid of $N$ grid points. The proposal distribution governing the selection of this grid point is uniform within the 2D spatial domain. A cell

nucleus is subsequently placed in that grid point and a new S-wave velocity is assigned. Bodin and Sambridge (2009) draw this new S-wave velocity from a Gaussian proposal distribution centered at the current velocity of the randomly selected grid point. A death step is the reverse of a birth step. Hence, it involves the random (uniform probability) selection of a grid point and subsequent elimination of the cell that contains it. A problem reported in the literature for the preceding birth/death proposals is the very low acceptance ratio (e.g., Dosso et al., 2014). This adversely affects the mixing of the transdimensional Markov chain and the efficiency with which the model space is being sampled.

To improve the acceptance probability of a birth/death step, several studies suggest proposing the velocity in a birth step using a uniform distribution over the prior range (e.g., Dosso et al., 2014; Xiang et al., 2018). This way the prior and proposal ratios cancel and the acceptance probability for the birth and the death step will be equal to the likelihood ratio, similar to equation 6, that is (Dosso et al., 2014; Xiang et al., 2018),

$$\alpha(\mathbf{m}'|\mathbf{m}) = \min\left[1, \exp\left(\frac{\phi(\mathbf{m}) - \phi(\mathbf{m}')}{2}\right)\right]. \quad (7)$$

This formulation is shown to have a higher acceptance ratio (e.g., Dosso et al., 2014; Xiang et al., 2018). This can be understood by considering a region in the subsurface with low sensitivity to the input data. Any perturbation in that region results in a likelihood ratio close to unity and hence is likely to be accepted. Consequently, when the sampled data are not equally sensitive to all regions in the subsurface, most of the accepted births/deaths occur in areas of the subsurface with rather low sensitivity to the data. In contrast to the original birth/death proposal scheme, this formulation does not result in a preference over simpler models, whereas this is desirable. In the following section, we therefore introduce a modified birth/death step that enhances the acceptance ratio while at the same time having a clear preference over simpler models (i.e., a preference over larger cells in case the likelihood ratio coincides for two Voronoi configurations).

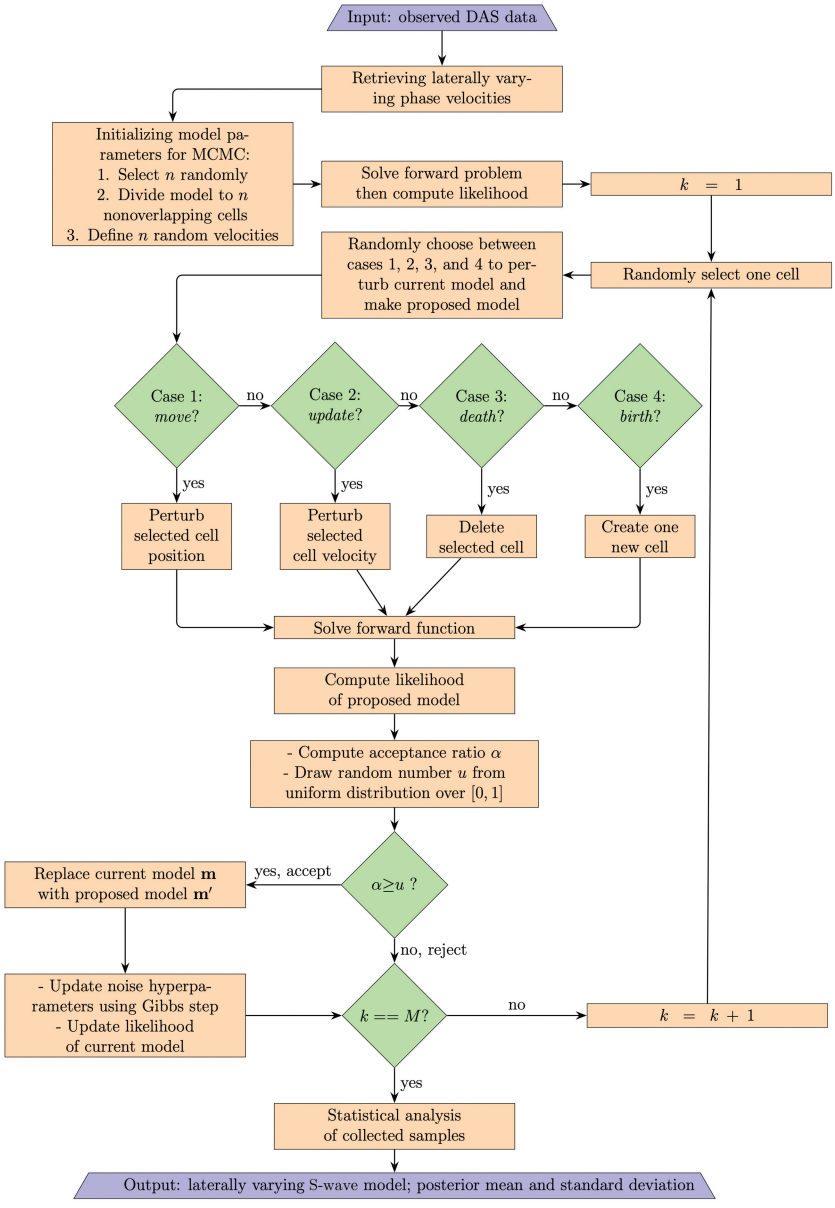


Figure 1. Flowchart illustrating the transdimensional MCMC method for generating $M$ samples to infer laterally varying S-wave velocity based on retrieved surface wave dispersion data.

*An improved birth/death scheme*

For the birth step, we randomly (uniform probability) select a point in the subsurface and make that the nucleus of a new cell. This new cell modifies the shape of the neighboring cells and constitutes parts of these cells. We compute the spatial average velocity $\overline{v}_i$ over the area of the proposed cell (before birth) using the dense underlying 2D grid of $N$ grid points. Then, we propose a new velocity $v'$ for the new cell using a Gaussian proposal distribution centered at $\overline{v}_i$ and with a standard deviation of $\sigma_v$. The proposal probability distribution associated with such a birth step reads

$$q(\mathbf{m}'|\mathbf{m}) = \frac{1}{N-n}\frac{1}{\sigma_v\sqrt{2\pi}}\exp\left(-\frac{(v'-\overline{v}_i)^2}{2\sigma_v^2}\right), \quad (8)$$

where $n$ is the number of grid points already acting as a cell's nucleus (prior to birth).

A death step is the reverse of birth step. Therefore, we consider the probability of randomly selecting a point that is contained in the birth cell. This probability is the size of the birth cell divided by the size of the spatial extent of the model. Approximating the cell size by the number of grid points inside it (i.e., $N_c$) and the size of the spatial domain by the total number of grid points in the model (i.e., $N$), the probability of such a proposal is

$$q(\mathbf{m}|\mathbf{m}') = \frac{\text{cell size}}{\text{domain size}} \approx \frac{N_c}{N}. \tag{9}$$

Using these two expressions, the proposal ratio for a birth step becomes

$$\left[\frac{q(\mathbf{m}|\mathbf{m}')}{q(\mathbf{m}'|\mathbf{m})}\right]_{\text{birth}} = \frac{N_c}{N}(N-n)\sigma_v\sqrt{2\pi}\,\exp\left(\frac{(v'-\overline{v}_i)^2}{2\sigma_v^2}\right). \tag{10}$$

Just as in Bodin and Sambridge (2009), the Jacobian coincides with unity for a birth/death step.

Substituting the prior ratio for a birth step (as derived by Bodin and Sambridge, 2009):

$$\left[\frac{p(\mathbf{m}')}{p(\mathbf{m})}\right]_{\text{birth}} = \frac{n+1}{N-n}\frac{1}{\Delta v}. \tag{11}$$

Equation 10, and the likelihood ratio (computed using equation 4) in equation 5, provides the acceptance probability of a birth step:

$$\alpha(\mathbf{m}'|\mathbf{m}) = \min\left[1, \frac{n+1}{\Delta v}\frac{N_c}{N}\sigma_v\sqrt{2\pi}\,\exp\left(\frac{(v'-\overline{v}_i)^2}{2\sigma_v^2} + \frac{\phi(\mathbf{m})-\phi(\mathbf{m}')}{2}\right)\right], \tag{12}$$

where $v'$ is the velocity of the new cell and $\overline{v}_i$ is the spatially averaged velocity in the area constituting the new cell before its birth. A death step is the reverse of the birth step; following a similar procedure as mentioned previously, we find the acceptance probability of a death step:

$$\alpha(\mathbf{m}'|\mathbf{m}) = \min\left[1, \frac{\Delta v}{n}\frac{N}{N_c}\frac{1}{\sigma_v\sqrt{2\pi}}\exp\left(-\frac{(v'-\overline{v}_i)^2}{2\sigma_v^2} + \frac{\phi(\mathbf{m})-\phi(\mathbf{m}')}{2}\right)\right], \tag{13}$$

where $v'$ is the velocity of the cell that was killed and $\overline{v}_i$ is the spatial average of the (new) velocities at the grid points that were located in that cell. One can see that the new formulation depends not only on the velocity of the birth/death cell but also on the size of the cell. It prefers giving birth to cells larger than the average size of all cells (i.e., $N_c/N$) and killing cells smaller than the average cell size. While creating a new cell or killing an available cell, the algorithm does not rely on the velocity of a single point (i.e., the cell nuclei) but considers the velocity of all points located inside the death/birth cell. This suppresses the effect of cells with anomalous velocities close to each other discussed in the previous section.

### *Noise parameterization and inference*

The data uncertainty plays a crucial role in the convergence of a Bayesian algorithm (Bodin et al., 2012; Rahimi Dalkhani et al., 2021). Ideally, this data uncertainty accounts for the uncertainty resulting from seismic noise as well as for the fact that the model used is a simplification of the true physics describing surface wave propagation. As we will explain in the "Application to DAS data recorded near Zuidbroek, Groningen" section, the application of the MOPA algorithm to multiple shots provides us with an estimate of the data uncertainty. However, this estimate does not take into account the second source of data uncertainty (i.e., inaccuracy inherent in the forward function). For this reason, similar to Bodin et al. (2012), we consider this data uncertainty to be an unknown and parameterize it as a linear relation:

$$\sigma_{ij} = a\sigma'_{ij}, \tag{14}$$

where $\sigma'_{ij}$ is the data uncertainty derived from the MOPA algorithm at location $x_j^{(c)}$ and discrete frequency $f_i$. Here, $a$ is a hyperparameter to take into account data, processing, and modeling-related errors. Bodin et al. (2012) use an additional MH step to infer this hyperparameter from the data automatically.

Here, following Andrieu et al. (1999), we propose a Gibbs sampling step (Gilks et al., 1995; Yildirim, 2012) to infer the noise hyperparameter ($a$) efficiently. Refer to the "Noise inference using a Gibbs sampler" section of Appendix A for detailed information on the algorithm. Compared with the MH step, the proposed Gibbs sampler is fast (no rejection) and unbiased. It does not need user-defined parameters except for a wide prior range for the hyperparameter $a$. The downside of the proposed algorithm compared with the MH step proposed by Bodin et al. (2012) is that the way we can parameterize the noise is limited. In other words, we can only assume that the noise level is a constant or it is a factor of a constant value such as what we discussed (i.e., $\sigma = a\sigma'$, where $\sigma'$ is known). If we want to parameterize the noise such as $\sigma = a\sigma' + b$, then our proposed method is not working and the MH step proposed by Bodin et al. (2012) is applicable.

### *Constraining the inversion using (borehole) S-wave logs*

It is possible to measure physical properties directly using borehole logging tools. In our case, two dedicated boreholes are drilled down to approximately 80 m depth. Using a P-S suspension logging tool, S-wave velocities are measured using approximately 400 Hz S waves. These S-wave velocity profiles can be incorporated into the transdimensional algorithm in two ways. First, the S-wave velocity profile can be used to constrain the prior probability and make it depth dependent. This can be achieved by assuming a Gaussian distribution centered at the measured S-wave velocity profile (see, e.g., Sen and Biswas, 2017). However, this approach needs the RJMCMC algorithm to be modified. In addition, it is difficult to define the prior mean in a Voronoi partitioned, variable parameterization of the model. An alternative approach is to use the S-wave velocity profiles to constrain the misfit function (see Wang, 2016, pp. 5) by the available data as

$$\phi(\mathbf{m}) = \left\|\frac{\mathbf{g}(\mathbf{m})-\mathbf{d}}{\sigma}\right\|^2 + \left\|\frac{\mathbf{V_m}-\mathbf{V_{ref}}}{\sigma_{bh}}\right\|^2, \tag{15}$$

where $\mathbf{V_m}$ is the S-wave velocity of the proposed model on a computational fine grid during MCMC sampling and $\mathbf{V_{ref}}$ is a reference S-wave velocity model defined on the same computational fine grid but based on the available borehole data. Because well logs have a much higher resolution than what can be achieved with surface wave methods, some smoothing of borehole S-wave velocity logs is likely necessary before it can be effectively used in building $\mathbf{V_{ref}}$. Here, $\sigma$ is the data uncertainty and $\sigma_{bh}$ is the reference model uncertainty. A lower $\sigma_{bh}$ imposes a stronger constraint on the

exploration of the model space, whereas a larger $\sigma_{bh}$ reduces this constraint. One can use a single (depth-independent) $\sigma_{bh}$ to constrain the misfit function close to the borehole for the whole model or make it location dependent. It depends on the level of information we have from the study area. In this study, we use a scalar single value for the whole model.

*Parallel tempering*

Parallel tempering is a technique used in MCMC sampling to improve the exploration of a probability distribution. In MCMC sampling, the Markov chain tends to become stuck in local modes of distribution, making it difficult to explore the entire distribution efficiently. To overcome this, one can resort to "simulated annealing." In simulated annealing, the likelihood function is smoothed using a temperature parameter $T$ (Sambridge 1999):

$$p(\mathbf{d}|\mathbf{m}) = A\,\exp\left(-\frac{\phi(\mathbf{m})}{2}\right)^{\frac{1}{T}} = A\,\exp\left(-\frac{\phi(\mathbf{m})}{2T}\right). \quad (16)$$

The temperature $T$ determines the roughness of the distribution that is being explored. Higher temperatures result in flatter distributions, allowing the Markov chain to move more easily between modes. At lower temperatures, chains tend to focus on specific modes.

Parallel tempering subsequently involves running multiple chains, each at a different temperature. The key idea of parallel tempering is to occasionally exchange samples (or temperatures) between chains. These exchanges allow for information to be shared between chains and help chains explore different parts of the distribution. Exchanging samples between chains at different temperatures effectively moves samples from flatter (higher temperature) chains to sharper (lower temperature) chains and vice versa. This helps the chains, collectively, to explore the entire distribution more efficiently and improves the rate of convergence to the target distribution. This is particularly beneficial when the distribution is multimodal. For details and additional information about the implementation, we refer readers to Sambridge (2014).

## APPLICATION TO SYNTHETIC DATA

To test the proposed 2D transdimensional approach, we consider a simple 2D synthetic model with lateral variation (Figure 2a). The wavefield is modeled using a 2D finite-difference elastic wave equation solver (SOFI2D) (Bohlen et al., 2016) assuming a free surface at the top of the model and vertical point forces. The source time function is a 10 Hz Ricker wavelet. The source is positioned at the model's surface, spanning the range from $x = 10$ to $x = 150$ and $x = 600$ to $x = 740$ with a source interval of 10 m. The velocity model is extended horizontally on both sides to fully encompass the area beneath the sources.

Because the straight fibers record the radial component of the surface waves, we use the horizontal component of the wavefield recorded at the surface of the synthetic model (Figure 2b). Although DAS records strain rate, the finite-difference modeling produces particle velocity. To ensure consistency, we convert the particle velocity ($V_x$) to strain rate using the following expression (adapted from Zulic et al. [2022] and Bakku [2015]):

$$\dot{\varepsilon}_{xx}\left(x-\frac{dx}{2}, x+\frac{dx}{2}\right) \approx \frac{V_x\left(x+\frac{dx}{2}\right) - V_x\left(x-\frac{dx}{2}\right)}{dx}, \quad (17)$$

where $\dot{\varepsilon}_{xx}$ is estimated to be the average strain rate obtained by DAS and $dx$ is equivalent to the gauge length of the DAS measurement.

In the synthetic experiment, the recorded surface wave on the horizontal component of the wavefield is the Rayleigh wave because the sources are in line with the DAS cable. We indicate the fundamental mode surface wave (R0), higher-modes surface waves (R+), and the direct body wave (DW) on the seismic record in Figure 2b. The *f-k* spectrum is shown in Figure 2c. The fundamental mode Rayleigh wave is dominant in Figure 2b–2d.

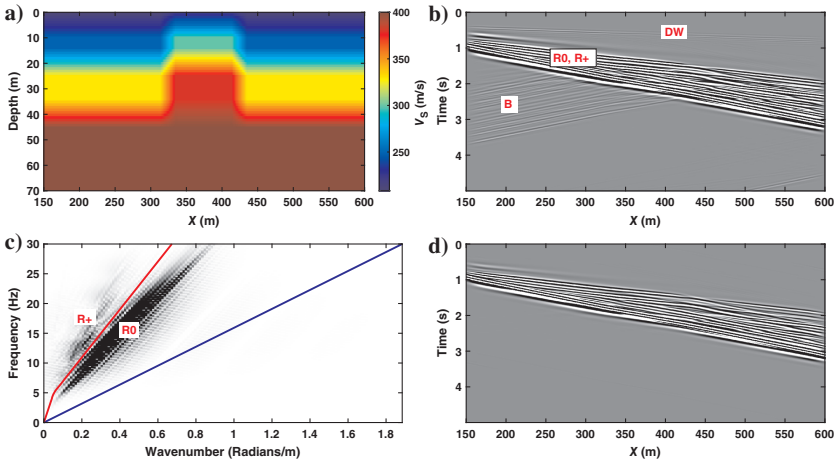


Figure 2. Surface wave spectral analysis of a synthetic active seismic record. (a) The prescribed synthetic model, (b) the horizontal component of the wavefield (i.e., strain rate) recorded at the surface for a source located at $x$ = 20 m, and (c) *f-k* spectrum. Fundamental mode surface waves (R0), higher modes surface waves (R+), back-scattered surface waves (B), and direct body waves (DW) are indicated in (b). (d) An isolated fundamental mode is retained after an *f-k* filter has been applied. The blue and red lines in (c) represent the corner frequencies of the applied (velocity) filter. The blue line represents a phase velocity of 100 m/s and the red line represents a frequency-dependent phase velocity between 260 and 600 m/s.

### MOPA of synthetic data

To obtain a reliable phase-versus-offset spectrum that is associated with the fundamental mode only, we isolate the fundamental mode (Figure 2d) by retaining the energy associated with fundamental mode surface wave velocities (indicated by blue lines in Figure 2c) and muting the rest of the spectrum (*f-k* filtering). The filtered data, after computation of the inverse transform, are shown in Figure 2d. For each discrete frequency $f_i$, the phases of the individual traces of the "cleaned" shot records are unwrapped (e.g., Weemstra et al., 2021), resulting in the $\phi - x$ spectrum. For the (*f-k* filtered) shot record in Figure 2, the (unwrapped) phase is shown as a function of offset for six different frequencies in Figure 3a.

The retrieved laterally varying dispersion relation using the MOPA is shown in Figure 3b for the

single shot record of Figure 2d. Here, we use a spatial window length $W(f_i)$ equal to two wavelengths, where the latter is computed using a reference phase velocity based on the (averaged) phase velocity retrieved through the application of MOPA to the whole shot record. This frequency dependency implies that $W$ decreases with increasing frequency. Linear regression using equation 1 subsequently results in frequency-dependent local wavenumbers for each $f_i$ and $x_j^{(c)}$ separately. These wavenumbers are then transformed into phase velocities using equation 2, yielding the set of laterally varying dispersion relations shown in Figure 3b.

To improve the quality of the recovered DCs, MOPA is conventionally applied to multiple shots, each located at a different (inline) position. In this synthetic experiment, we generate 30 shot records with sources located between 10–150 and 600–740 m and with a source spacing of 10 m. In addition, an *f-k* filter is applied to each (Fourier-transformed) shot record to facilitate a reliable phase analysis by isolating the fundamental mode. Subsequently, laterally varying DCs are estimated by applying MOPA to each shot record separately. At each position $x_j^{(c)}$, this results in 30 independently estimated DCs. The average of these 30 sections is shown in Figure 3c. The associated standard deviation is shown in Figure 3d, which can be considered as a measure of the uncertainty of the recovered $c_p(f_i, x_j^{(c)})$.

Figure 3e shows the (true) theoretical location-dependent phase velocities as a reference. These are computed by taking the true 1D S-wave velocity profile at each location and then computing the theoretical DC using the aforementioned reduced delta matrix method (Buchen and Ben-Hador 1996; Wu et al., 2019). Figure 3f shows the actual phase velocity error computed based on the theoretical DC (i.e., Figure 3e) and the MOPA-derived phase velocities (i.e., Figure 3c). Figure 3c and 3e–3f shows that lower frequencies (less than 3 Hz) are associated with higher uncertainties and deviate from the theoretical dispersion relation. This is due to the low amplitude of the source time function (i.e., a 10 Hz Ricker wavelet) at those frequencies. In addition, the MOPA algorithm does not cover the regions close to the ends of the line due to the spatial windowing: because this window length $W$ is larger at lower frequencies, lower frequencies are sampled over a shorter spatial interval in Figure 3b and 3c.

## Transdimensional 2D inversion of synthetic data

To assess the performance of the proposed algorithm, the theoretical phase velocities (Figure 3e) and the recovered phase velocities (Figure 3c) are used as input to the proposed 2D transdimensional algorithm. In the next two sections, we present the results of these tests separately for the two sets of phase velocities.

### *Inverting theoretical phase velocities*

We first add random zero-mean Gaussian noise with a standard deviation of 10 m/s to the theoretical phase velocities shown in Figure 3e. The resulting noisy phase velocities (shown in Figure 4a) are then used as the input to the proposed inversion algorithm. We sample the posterior probability distribution with 20 parallel chains, each sampling 500,000 samples. Ten chains have a temperature of one and the other 10 chains have a temperature logarithmically spaced between 2 and 100. The tempering (exchanging temperature values between chains) starts at iteration 75,000. The initial samples are generated randomly from the prior range with a velocity increasing monotonically with depth. A sample initial model is shown in Figure 4b. The true velocity profile at $x = 150$ m is extended horizontally and is considered as the reference model while constraining the misfit function. The model uncertainty ($\sigma_{bh}$ in equation 15) is assumed to be 100 m/s. The S-wave velocity prior is a uniform prior between 150 and 600 m/s. For the data uncertainty (noise level), we assume an unknown noise hyperparameter ($a$ in equation 14) to be estimated by the proposed Gibbs step during the MCMC sampling. By prescribing $\sigma'_{ij} = 1$ (see equation 14) and given that $\sigma_{ij} = 10$, $a$ can be expected to approach 10 (asymptotically). The first 200k samples are discarded as the burn-in phase. Then, we retain a sample every 100 iterations. The posterior mean and standard deviation are then computed based on the retained samples with a temperature of one (i.e., $T = 1$). Figure 4c and 4d shows two samples at iteration 50,000 (burn-in phase) in two chains with temperatures of $T = 1$ and $T = 100$, respectively. This clearly shows the effect of the temperature on the sampling.

Figure 5 shows the results of the transdimensional inversion. Figure 5a shows how the number of cells varies as a function of iteration and temperature. The initial temperature of each chain is indicated by the color of each curve. The number of cells stabilizes after a few thousand iterations with the higher temperature chains (red ones) having a lower number of cells. After the start of parallel tempering (i.e., the exchange of temperature values after iteration 75,000), the number of cells associated with the chains initially at lower temperatures reduces and the number of cells associated with the chains initially at higher temperatures increases, both effectively converging to the same range of number of cells. This

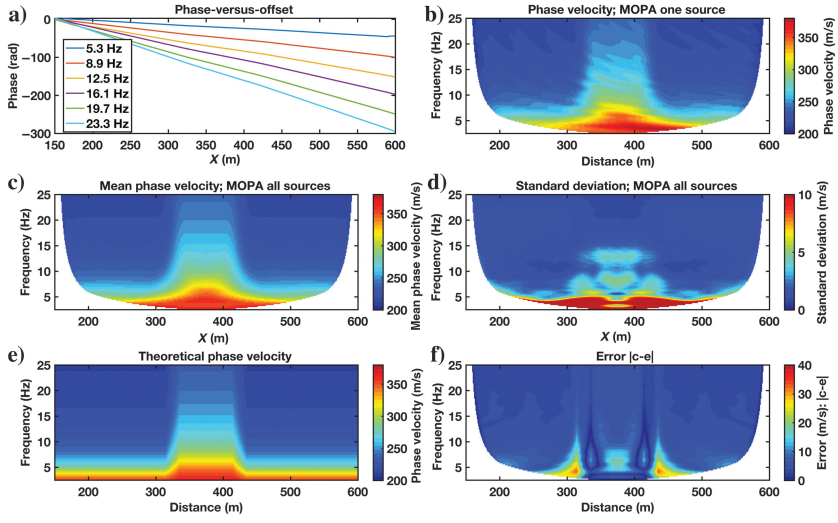


Figure 3. Phase velocity retrieval using MOPA: application to synthetic recordings. (a) Phase versus offset for six discrete frequencies of the filtered shot record shown in Figure 1d. (b) Phase velocities $c_p(f_i, x_j^{(c)})$ retrieved from one single shot record. (c) Mean local phase velocities retrieved from shots with sources at 30 different locations. (d) Standard deviation corresponding to (c). (e) Theoretical (true) laterally varying phase velocities. (f) The phase velocity error is computed based on (c) the MOPA-derived phase velocity and (e) the theoretical phase velocities.

demonstrates the convergence of the chains and also highlights the effect of temperature on the exploration of the model space.

Figure 5b shows the inferred noise level at different iterations. Not surprisingly, $a$ converges to the standard deviation of the additive random noise (i.e., 10 m/s) for chains without tempering (i.e., $T = 1$). For the tempered chains, the inferred noise level is increasing for higher temperature values. Increasing temperature leads to a more global search of the model space and leads to a higher acceptance rate. This means that models with higher uncertainties are allowed in the collected samples. This explains why the algorithm infers a higher noise level in chains with higher temperatures.

Figure 5c shows that the mean of the postburn-in retained samples associated with a temperature of one nicely correlates with the true S-wave velocity (Figure 2a). The layer interfaces and the velocity structure are recovered correctly, even though it is a bit smoother than the true velocity model. The smoothing is mainly due to the additive random noise. Figure 5d shows the posterior standard deviation computed from the retained postburn-in samples with a temperature of one. As expected, the layer interfaces appear with higher uncertainties. It should be understood that, by using the true local DCs, these results overestimate the performance of the proposed Bayesian approach. That is, in application to field data, we do not have the local (1D) phase velocities at our disposal. Instead, we rely on the MOPA-derived DCs, which approximate the true dispersion phase velocity dispersion in the sense that wavefield amplitudes are ignored (Wielandt 1993). In the next section, we therefore apply our algorithm to DCs estimated through MOPA applied to (finite-difference) modeled wavefields.

### *Inverting MOPA-derived phase velocities*

After the successful recovery of the true S-wave velocity from the theoretical phase velocities, the MOPA-derived local phase velocities are now used in the proposed 2D transdimensional inversion algorithm. Then, we use 20 independent chains to sample the posterior, each sampling 500,000 models. The initial model of each chain is generated randomly with a randomly selected number of cells and based on a randomly chosen location. We only assume an increasing velocity with depth for the initial model (Figure 4a). Then, we discard the first 200,000 samples as the burn-in period. Then, samples are retained at every 100 iterations to avoid collecting correlated samples. The retained samples with a temperature of one are then used for the calculation of the posterior mean (Figure 6c) and the posterior standard deviation (Figure 6d).

Figure 6c shows that the proposed algorithm recovers a smooth version of the true S-wave velocity model in Figure 2a. The "smoothing" is predominantly due to the approximation inherent in the MOPA algorithm. The model uncertainty shown in Figure 6d is higher at the layer interface at a depth of approximately 20 m. This occurs because the layer interfaces can be sampled by the velocities of the layers above and below, leading to increased standard deviation.

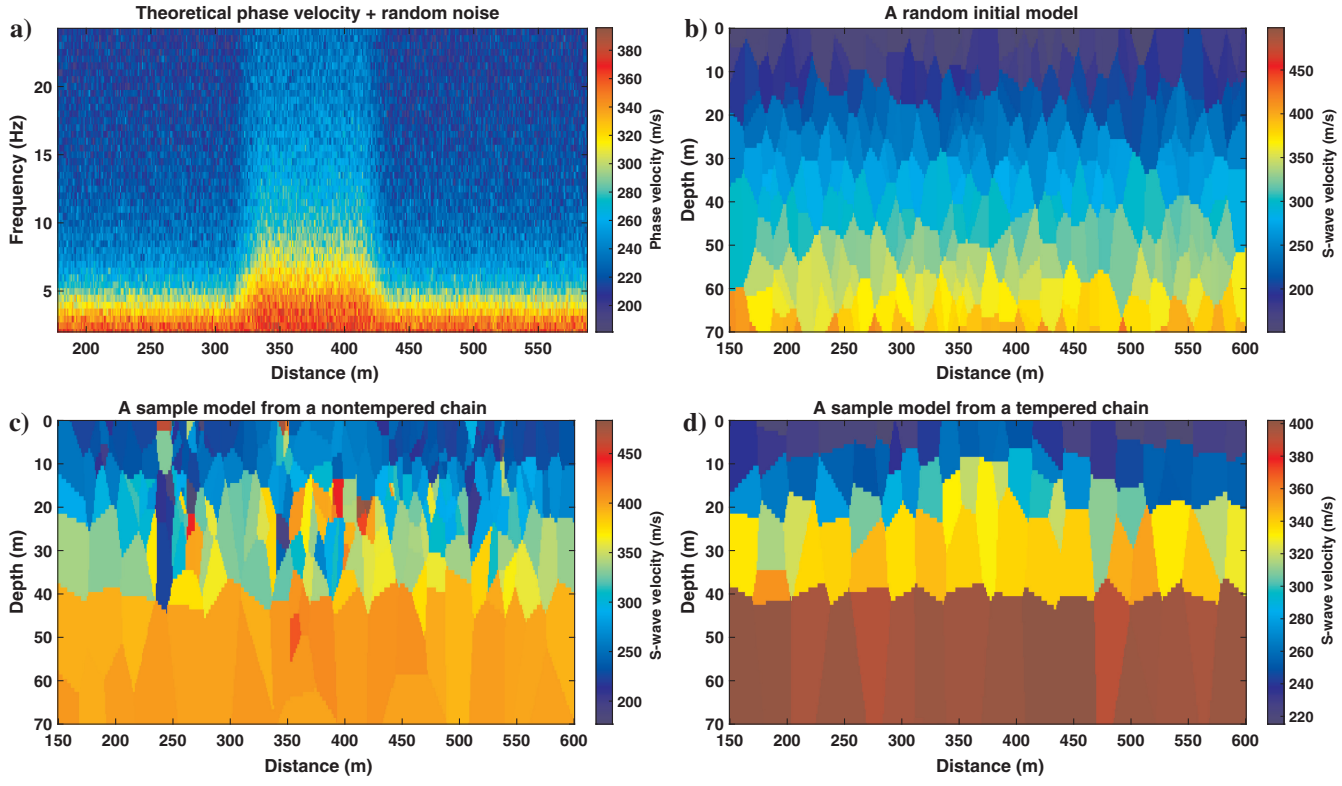


Figure 4. (a) The theoretical phase velocity after the addition of Gaussian noise with the standard deviation set to 10 m/s. (b) An initial sample (i.e., model) is generated randomly with an increasing S-wave velocity by depth. Two samples collected after 50,000 iterations are shown in (c) for a cold chain with $T = 1$ and (d) for a hot chain with $T = 100$, showing that higher temperatures result in coarser models (and hence also fewer Voronoi cells).

*Inverting phase velocities using a linearized least-squares algorithm*

We compare our transdimensional scheme with a linearized least-squares inversion technique, which inverts the frequency-dependent phase velocities at each location to obtain a 1D S-wave velocity depth profile (for details, see Xia et al., 1999). By applying the inversion algorithm at multiple locations and assembling the resulting 1D profiles, we generate a 2D S-wave velocity model of the subsurface. Figure 7 shows the results of the least-squares inversion, applied to the noisy theoretical phase velocities (Figure 4a) and the phase velocities derived from MOPA (Figure 3c). A comparison between the S-wave velocity profiles obtained using the proposed transdimensional approach (Figure 5c) and the least-squares method (Figure 7a) reveals that the transdimensional approach recovers a laterally correlated and smoothed model, while still capturing sharp lateral and vertical variations in S-wave velocity. In contrast, the velocity model obtained from the least-squares method requires additional lateral smoothing. Moreover, the transdimensional algorithm provides valuable insight into model uncertainty, particularly in highlighting regions of higher uncertainty along layer interfaces.

Comparing the inversion results of the MOPA-derived phase velocities, the least-squares and transdimensional algorithms produce similar outcomes (see Figures 6c and 7b, respectively). This similarity arises because the input DCs are already smoothed by the inherent characteristics of the MOPA algorithm. However, the transdimensional algorithm offers enhanced lateral and vertical resolution. In addition, it provides the advantage of estimating model uncertainties, offering valuable insights, especially regarding the layering and sharp velocity variations within the model. Furthermore, the transdimensional approach is less influenced by user-defined parameters compared with the least-squares algorithm, which relies on specific model parameterization and regularization choices.

## APPLICATION TO DAS DATA RECORDED NEAR ZUIDBROEK, GRONINGEN

In this section, we discuss the application of the proposed Bayesian algorithm to data recorded using a straight-fiber DAS system. We first introduce the data. We subsequently recover the local phase velocities, which we then exploit to recover a 2D S-wave velocity model of the subsurface. In the last section, we compare the recovered S-wave velocity sections with S-wave

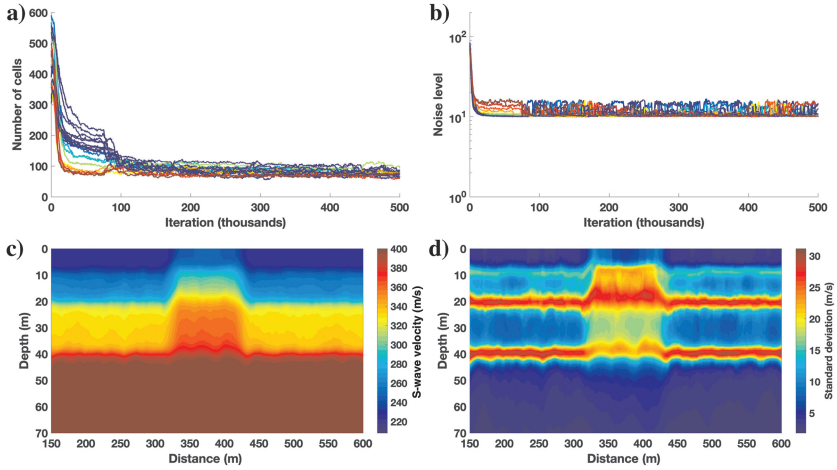


Figure 5. Transdimensional inversion results by using the noisy theoretical phase velocities (Figure 3a) as the input data. (a) Number of cell variations by iteration at 20 different chains. The color of each line indicates the initial temperature of the corresponding chain with red for the highest temperature (i.e., $T = 100$) and blue for the coldest chain (i.e., $T = 1$). (b) The variation in inferred noise level (standard deviation) by iteration at 20 different chains. The $y$-axis is plotted in a log scale for better visibility of variations. The color of each line is similar to (a) indicating the initial temperature of each chain. (c) The posterior mean of the collected samples with a temperature of one from 20 parallel chains. (d) The posterior standard deviation of the retained samples with a temperature of one. The color scale in (c) is the same as for the true model in Figure 1a.

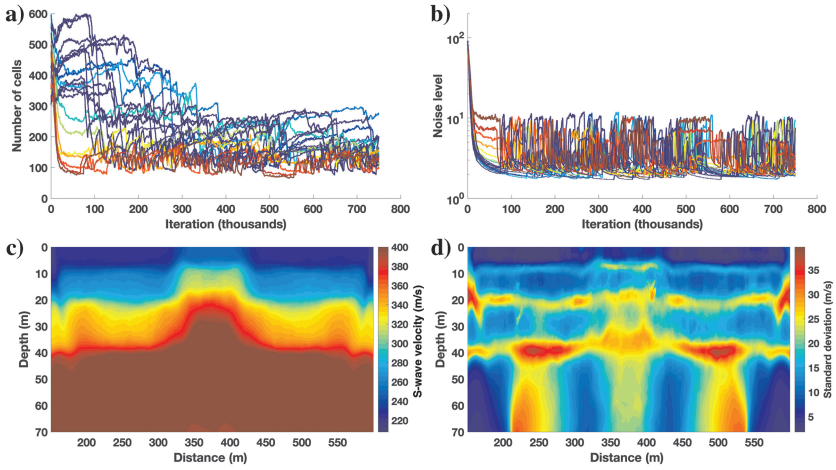


Figure 6. (a–d) The same as Figure 4a–4d, respectively, but using the MOPA-derived phase velocities (Figure 2c) as input. The color scale in (c) is the same as for the true model in Figure 1a.

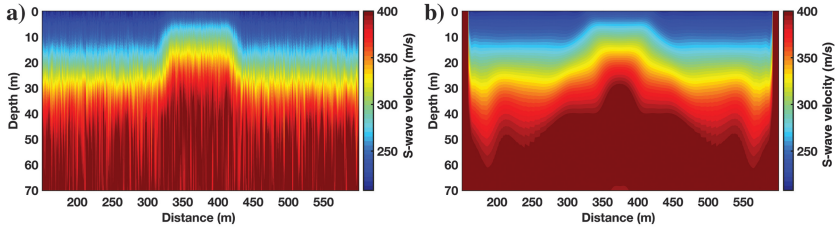


Figure 7. The S-wave velocity profiles obtained using a least-squares inversion algorithm applied to (a) the noisy theoretical phase velocities (Figure 3a) and (b) the MOPA-derived phase velocities (Figure 2c). The color scales are the same as for the true model in Figure 1a.

velocity profiles measured along two boreholes positioned on the acquisition line.

## DAS data characteristics

We apply the proposed methodology to DAS data obtained in the province of Groningen in the north of the Netherlands. The top 800 m of the subsurface mainly consists of unconsolidated sediments in this region, with the uppermost layers being of Pleistocene age (down to 25 m, but varying from one place to the other; Kruiver et al., 2017).

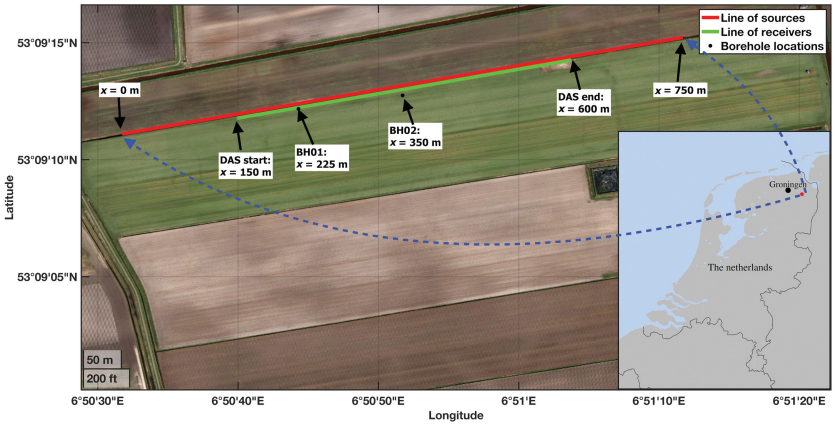


Figure 8. The acquisition setup of the DAS experiment near Zuidbroek, Groningen. The solid red line represents the source line, which has a length of 750 m. The green line represents the DAS straight fiber buried at a depth of 2 m and with a length of 450 m. The position of the first source line is defined as $x = 0$ with the end of the source line then being $x = 750$ m. The DAS fiber is buried between $x = 150$ and 600 m. Two boreholes are drilled to a depth of 80 m at $x = 225$ m and $x = 350$ m to measure the S-wave velocity directly.

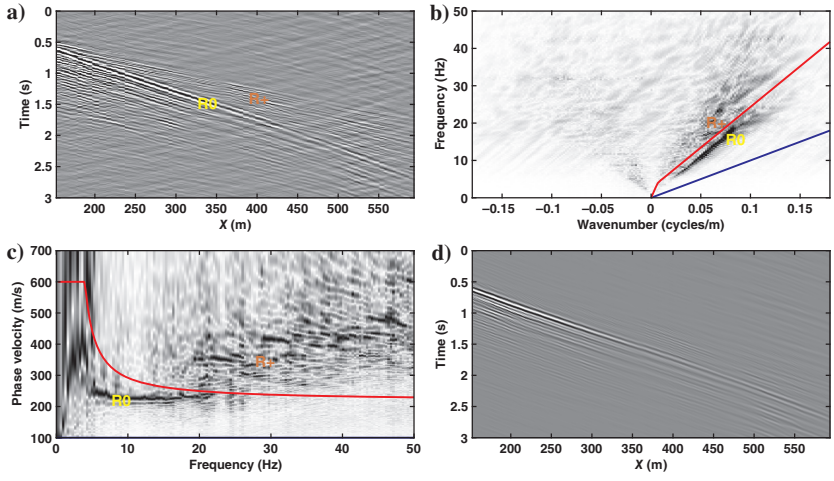


Figure 9. (a) A common-shot record, (b) its corresponding *f-k* amplitude spectrum, and (c) its corresponding dispersion image. The source is located at $x = 10$ m. The fundamental mode and higher modes are indicated by R0 and R+, respectively. The blue line represents a phase velocity of 100 m/s and the red line represents a frequency-dependent phase velocity between 220 and 600 m/s. Higher-mode surface waves are effectively removed by retaining the *f-k* spectrum between the blue and red lines (*f-k* filter). The resulting (time-domain) fundamental mode surface wave shot records are shown in (d).

The data are obtained with fibers as part of a DAS system. Figure 8 shows the acquisition setup of the DAS recording system. Different types of fibers are used, namely straight and helically wound fibers (for more details, see Hasani and Drijkoningen [2023]). However, we opt for the straight-fiber data as it showed the highest sensitivity to the surface waves. The source used is an electrically driven vertical seismic vibrator (Noorlandt et al., 2015) generating two shots per position from $x = 0$ to $x = 750$ every 2 m. The straight fiber is buried at a depth of 2 m with a length of 450 m from $x = 150$ to 600 m. More information on the acquisition can be found in Hasani and Drijkoningen (2023). The (receiver) spacing of the recordings is 1 m with a gauge length of 2 m, and a time sampling rate of 2 ms is used in this study.

All shots positioned on the recording line (i.e., source location between $x = 150$ and 450 m) are split into two off-end shot records to be used in the MOPA algorithm. However, to take into account the near-offset effect (see Park et al., 1999), any trace having an offset smaller than 80 m (i.e., half of the expected maximum wavelength) is discarded. In addition, after removal of the near offsets, any shot record that has a length of less than 50 m is discarded. This is to make sure that there is sufficient data for the *f-k* filtering and then the calculation of phase versus offset.

Figure 9 shows a sample shot gather of the DAS data. The *f-k* and $c_p$-*f* spectra also are provided for a better understanding of the data. The straight fiber records the radial component of the wavefield. Because the vertical source is in line with the fiber (i.e., receivers), the recorded surface wave in the radial direction can be interpreted as the Rayleigh wave (assuming low-amplitude oblique incident Rayleigh and Love waves, i.e., little surface wave scattering, and low-amplitude oblique incident body waves in the *f-k* domain of interest). Indeed, the shot record appears to be dominated by the fundamental mode Rayleigh wave indicated by **R0**. The fundamental mode is easily detectable in the frequency range of 4–20 Hz in *f-k* and $c_p$-*f* spectra. The higher modes also are clearly visible in shot records and their corresponding spectra. We have indicated higher modes by **R+** because more than one higher mode is visible in the *f-k* and $c_p$-*f* spectra and because it is difficult to separate them. The colored lines in the *f-k* spectra represent phase velocities used to design a velocity filter for isolating the fundamental mode. The velocity lines also are depicted on the $c_p$-*f* spectra for the reader's reference. The red line separating the fundamental mode from higher modes is velocity dependent. The *f-k* spectrum between the blue and the red line is preserved and the rest of the spectrum is filtered out (*f-k* filtering). The filtered record is shown in Figure 9d and is dominated by the fundamental mode Rayleigh wave. We have applied this velocity filter to all shot records.

## Borehole data

In this study, two open boreholes are drilled down to a depth of 80 m at $x = 225$ m and $x = 350$ m. The (vertical) S-wave velocity and the P-wave velocity are measured directly using a PS suspension logging tool (Geovista Digital P&S Sonde). In addition to these seismic velocities, the bulk electrical conductivity and the gamma radiation are measured. The measured logs are shown in Figure 10. From 2 to 10 m below ground level, the subsurface is predominantly sandy. The relatively low electrical conductivity values down to 10 m depth indicate fresh water, and the relatively low gamma-ray values in the same depth range suggest low clay content. The main feature observable from the logs is a clear reduction of S-wave velocity between 10 and 20 m together with an increase in gamma ray and conductivity, especially in Figure 10a. The reduction in S-wave velocity is due to the higher clay content, apparent from the conductivity and gamma-ray readings (solid red and black lines, respectively) being higher than above and below that depth range. From 20 to approximately 55–60 m, a gradual fining-up trend is present in both boreholes, which is intersected by some more clayey units, for example, as shown in Figure 10a, at approximately 35 m. From 55 to 60 m, a heterogeneous clayey unit can be recognized in both boreholes. Below, until the bottom of the borehole, a second gradual fining-up sequence is present.

The S-wave logs are used to constrain the misfit function as explained in the "Constraining the inversion using (borehole) S-wave logs" section. To that end, we use moving averages of the S-wave velocity obtained at the two boreholes as 1D reference velocity profiles. We extend these 1D S-wave velocity profiles horizontally to build a 2D reference model for constraining the misfit function. For the uncertainty of this reference model, we opt for a constant value of $\sigma_{bh} = 150$ m/s.

To compute the surface wave DCs theoretically, we need the S-wave velocity ($V_S$), the P-wave velocity ($V_P$), and density ($\rho$). However, the S-wave velocity is predominantly controlling surface wave phase velocities, and therefore the effect of $V_P$ and $\rho$ is usually ignored (e.g., Wathelet, 2008). Here, we use the velocity logs to obtain an estimate of the $V_P/V_S$ ratio to be used in the theoretical calculation of the DCs. To that end, we compute moving averages of the S-wave velocity profile and the P-wave velocity profile. A depth-dependent $V_P/V_S$ ratio is subsequently computed based on these smoothed curves. We then take the average of this curve as the $V_P/V_S$ ratio that dictates the $V_P$ in our Bayesian algorithm. This average $V_P/V_S$ turns out to be close to five.

## MOPA of Zuidbroek data

After isolating the fundamental mode (Figure 9d), we apply the MOPA algorithm to all shot records extracted from the DAS data. Figure 11 shows the results of the MOPA method applied to the field DAS data to retrieve the DCs. The unwrapped phase versus offset for seven frequency components of a single shot record (Figure 9b) is shown in Figure 11a. The retrieved laterally varying DCs are shown in Figure 11b. The shot record is somewhat noisy, which manifests itself in relatively rapidly varying gradients of the phase-versus-offset curves. A smoother and more reliable DC is derived by repeating the process for multiple shot records. Figure 11c shows the average laterally varying DCs derived from all shot records. The uncertainty (quantified by means of a standard deviation) is shown in Figure 11d.

## Transdimensional 2D inversion of Zuidbroek data

The retrieved laterally varying phase velocities (Figure 11c) serve as input to the 2D transdimensional algorithm. We run 20

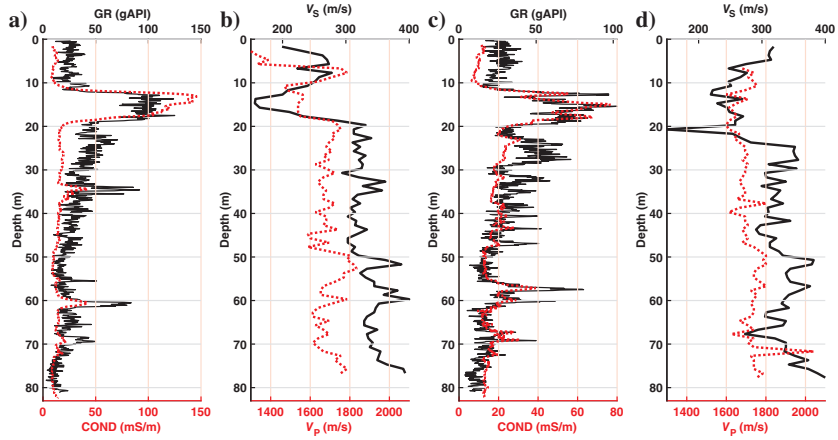


Figure 10. The measured logs of (a and b) first borehole at $x = 220$ m and (c and d) second borehole at $x = 350$ m. (a and c) Conductivity (COND; dashed red curve, bottom axis) from induction-log readings and gamma ray (GR; black curve; top axis), respectively. (b and d) The S-wave velocity profile ($V_S$; black curve; top axis) and P-wave velocity profile ($V_P$; dashed red curve, bottom axis), respectively.

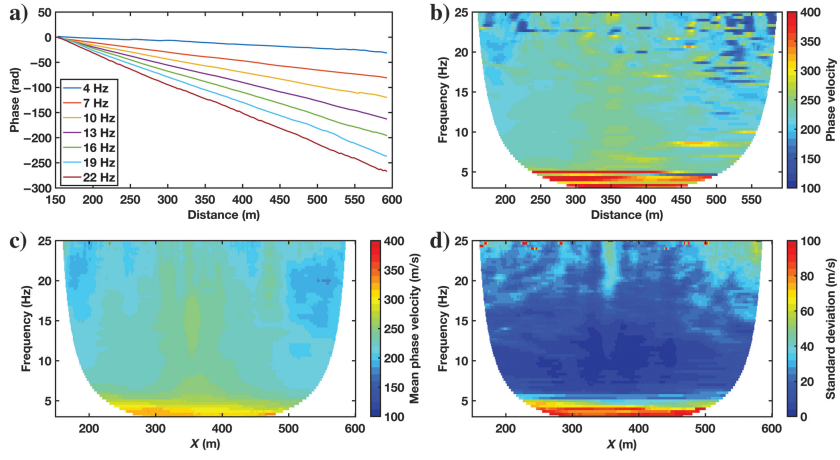


Figure 11. The MOPA applied to the DAS-derived shot records to estimate lateral S-wave velocity variations in the subsurface. (a) Unwrapped phase versus offset at seven different frequencies (different colors) for the filtered seismic record shown in Figure 8d. (b) Laterally varying phase velocity retrieved from the single shot record of Figure 8d. (c) Mean of the laterally varying DCs retrieved from all shots. (d) Standard deviation corresponding to (c).

independent MCMC chains in parallel, with each sampling 750,000 models. Here, 10 chains have a temperature of one and 10 chains have their temperatures logarithmically spaced between 2 and 100. Tempering starts at iteration 75,000. The initial model at each chain is selected randomly, but velocity increases monotonically with depth. Figure 12 shows the variation in the dimension of the model space (Figure 12a) and also the progression of the inferred noise level (Figure 12b). Similar to the synthetic data, chains with a higher initial temperature converge to a lower number of cells. By interchanging temperatures between chains, the number of cells converges to a lower range in (initially) cold chains, effectively preventing them from being stuck in local modes. For the inference of the noise level, we use the MOPA-derived phase velocity uncertainties (Figure 11d) as $\sigma'_{ij}$ in equation 14. We subsequently infer $a$ using the proposed Gibbs step. The first 250,000 samples of each chain are discarded as the burn-in phase. To avoid correlated samples, every 100th sample is retained. We then use the retained samples associated with chains with a temperature of one to approximate the posterior distribution. From the posterior distribution, we compute the pointwise averaged phase velocities and pointwise standard deviations, which we refer to as the posterior mean and standard deviation.

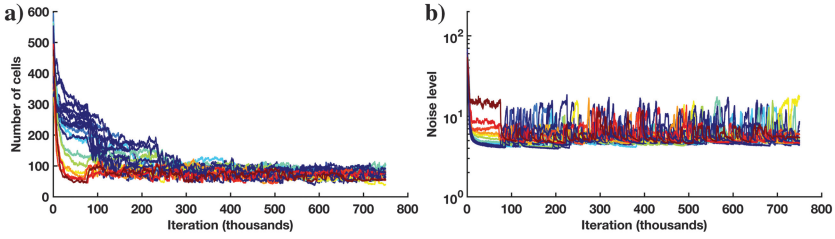


Figure 12. Chain statistics of the 2D transdimensional algorithm with (field-data-derived) phase velocities serving as input data (see Figure 10c). (a) Number of cells as a function of sample number for all 20 chains. The color of each solid line indicates the initial temperature of the corresponding chain with red corresponding to the highest temperature (i.e., $T = 100$) and blue corresponding to the coldest chain (i.e., $T = 1$). (b) The variation in inferred noise level (standard deviation) as a function of sample number for all chains. The vertical axis is plotted using a log scale to visualize the variations more clearly. Similar to (a), the color of each line corresponds to the initial temperature of that chain.

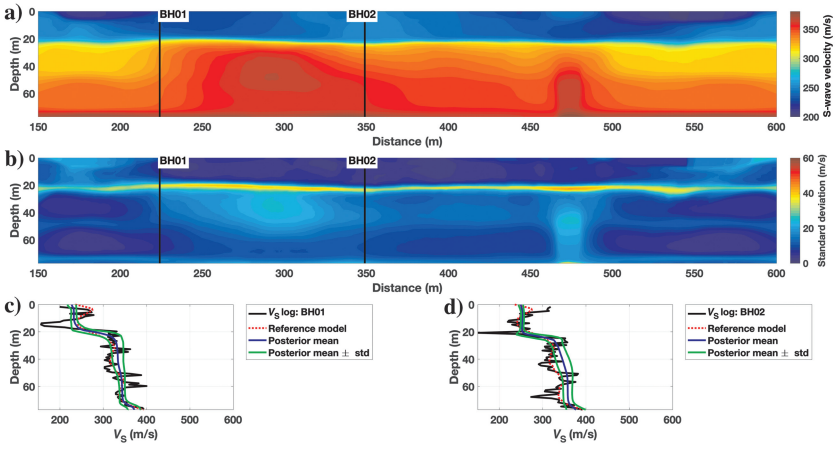


Figure 13. Result of the application of the 2D transdimensional algorithm to the DAS-derived phase velocities. (a) Recovered 2D S-wave velocity section (i.e., posterior mean), (b) recovered model uncertainty (i.e., posterior standard deviation; std), and comparison with the S-wave velocity profile along the (c) first and (d) second borehole.

Figure 13 shows the recovered S-wave velocity section and its corresponding uncertainty using the proposed 2D transdimensional method. The S-wave velocity profiles from the well logs also are compared with the posterior mean (Figure 13c and 13d): compared with the S-wave velocity logs, the inverted S-wave velocity is relatively smooth. A clear interface is located at a depth of approximately 20 m and results in a high model uncertainty at that depth (Figure 13b). This is in agreement with the well-log data presented in Figure 10. However, the algorithm fails to recover the velocity variation within the top 20 m. This is due to the high uncertainty of the MOPA-derived phase velocities and also the high inferred noise hyperparameter $a$. In particular, we attribute this to phase velocities at higher frequencies not being recovered very well due to the interference of higher modes. Moreover, the MOPA algorithm uses a spatial window while retrieving distance-dependent phase velocities, which leads to a laterally smooth phase velocity map (see, e.g., Figure 3c). In addition, the MOPA-derived phase velocities (Figure 11c) at the sides of the model have fewer frequency components and are therefore associated with higher uncertainties (reflected in Figure 13b). Finally, we note that at the lower end of the frequency spectrum, the MOPA-derived phase velocities exhibit relatively large uncertainties due to the limited excitation of lower frequencies by the vibroseis (see Figure 11d).

## DISCUSSION

Several points need to be discussed. First, when comparing the well-log data with the recovered S-wave velocities in Figure 13, it is evident that the recovered S-wave velocity is a smoothed version of the S-wave velocity logs, as expected. The layer interface at a depth of 20 m is well resolved, indicated by the sharp change in S-wave velocity and reflected in the anomalous variation in the model uncertainty map.

Second, the limited sampling toward the end of the line is inherent to the MOPA algorithm we use in this study. The quality of the DCs at these locations might be improved by the tomography-derived phase velocity retrieval algorithm (Barone et al., 2021). In addition, the MOPA-derived phase velocity estimates are affected by higher modes, especially at higher frequencies. The windowing also laterally smooths the retrieved phase velocities, prohibiting the recovery of a lateral high-resolution S-wave velocity structure. This might be improved by using the common-midpoint crosscorrelation algorithm (Hayashi and Suzuki 2004) for the recovery of the distance-dependent phase velocities but is beyond the scope of this study.

Third, data uncertainty play a crucial role in the convergence of our Bayesian algorithm (Bodin et al., 2012; Rahimi Dalkhani et al., 2021). As we explained previously, the MOPA algorithm provides us with an estimate of the data uncertainty (Figure 3f). In this study, we use this MOPA-derived uncertainty in combination with a hyperparameter during the MCMC sampling

of the posterior. We assume one hyperparameter for all frequencies. In case the true data uncertainty varies with frequency, a (smooth) frequency-dependent hyperparameter may improve the inversion result by allowing the data uncertainty to vary with frequency.

Finally, in terms of computation time, the proposed 2D transdimensional algorithm is comparable with independent 1D inversion of the DCs. This is because in the proposed 2D transdimensional algorithm, at each step of the MCMC, we perturb a small portion of the model space. Then, we compute the forward function (i.e., the primary source of the computational demand) only at the updated part of the model space. This reduces the computational time significantly. The added values of the proposed 2D transdimensional scheme are the enhanced lateral correlation and the reduced solution nonuniqueness.

## CONCLUSION

This study evaluates a 2D transdimensional inversion approach on synthetic seismic data and field data from DAS to recover subsurface S-wave velocity profiles. Initially, the method is applied to theoretical phase velocities and those obtained from MOPA on synthetic wavefield data, enabling an assessment of the algorithm's accuracy and robustness. The transdimensional inversion effectively captures lateral and vertical variations in velocity while providing model uncertainty estimates, especially near layer boundaries. Compared with traditional linearized least-squares inversion, the transdimensional method produces smoother, laterally coherent models without strict parameterization or regularization needs. Although both methods yield similar results when MOPA-smoothed data are used, the transdimensional approach offers improved resolution and richer insights into model uncertainty, enhancing its utility for detecting layering and sharp velocity changes in the subsurface.

The study further explores the potential of Rayleigh waves recorded with DAS using straight fibers, combined with the 2D transdimensional inversion, to construct a 2D S-wave velocity profile down to approximately 60 m. First, laterally varying phase velocities are estimated via MOPA, after which the 2D transdimensional inversion is applied to jointly invert all available DCs. The results show a smoothly varying S-wave velocity model along the acquisition line, with the posterior mean profile clearly delineating a prominent layer interface at a depth of approximately 20 m. This boundary is characterized by an abrupt increase in S-wave velocity and is associated with high model uncertainty at that depth, consistent with borehole log data that also indicate rapidly increasing velocities at the same depth.

## ACKNOWLEDGMENTS

We thank K. Wapenaar for his meticulous review, and his feedback certainly improved our manuscript. This research has received funding from the European Research Council (ERC) under the European Union's Horizon 2020 research and innovation program (grant no. 742703). The authors acknowledge the use of computational resources of the DelftBlue supercomputer, provided by Delft High Performance Computing Centre (DHPC).

## DATA AND MATERIALS AVAILABILITY

Data associated with this research are available and can be obtained by contacting the corresponding author.

## APPENDIX A

## NOISE INFERENCE USING A GIBBS SAMPLER

Gibbs sampling is a Markov chain that samples the posterior probability density of a parameter. It uses the conditional posterior distribution of the parameter with the remaining variables fixed to their current values (Yildirim, 2012). Accordingly, to sample the hyperparameter $a$, we need to derive its posterior distribution ($p(a|\mathbf{d})$) under the condition of the model $\mathbf{m}$. Applying Bayes' theorem, the posterior distribution ($p(a|\mathbf{d},\mathbf{m})$) is proportional to the product of the likelihood ($p(\mathbf{d}|a,\mathbf{m})$) and the prior (Gelman et al., 2014)

$$p(a|\mathbf{d},\mathbf{m}) \propto p(\mathbf{d}|a,\mathbf{m})p(a), \tag{A-1}$$

where the prior on $a$, $p(a)$, is assumed to be uniform (within bounds). Here, $p(\mathbf{d}|a,\mathbf{m})$ can be replaced by the likelihood function for a specific $a$ and the known model $\mathbf{m}$. It is worth mentioning that $\mathbf{m}$ is treated as a known constant in equation A-1, not a parameter that varies. The likelihood and the prior depend on $a$, and the hyperparameter posterior distribution is updated based on the observed data $\mathbf{d}$ and the known model $\mathbf{m}$.

In our case, the likelihood function in equation 4 reads

$$p(\mathbf{d}|\mathbf{m}) = \prod_{i=1}^{N_f}\prod_{j=1}^{N_x}\left(\frac{1}{\sqrt{2\pi}\sigma_{ij}}\exp\left(-\frac{(g_{ij}(\mathbf{m})-d_{ij})^2}{2\sigma_{ij}^2}\right)\right), \tag{A-2}$$

where $N_x$ is the number of locations $x_j^{(c)}$ for which a DC is estimated (i.e., $j = 1, 2, \ldots, N_x$). Data point $d_{ij}$ is the phase velocity at discrete frequency $f_i$ and location $x_j^{(c)}$. Inserting this likelihood function in equation A-1 gives

$$p(a|\mathbf{d},\mathbf{m}) \propto \prod_{i=1}^{N_f}\prod_{j=1}^{N_x}\left(\frac{1}{\sigma_{ij}\sqrt{2\pi}}\exp\left(-\frac{(g_{ij}(\mathbf{m})-d_{ij})^2}{2\sigma_{ij}^2}\right)\right)p(a). \tag{A-3}$$

By substituting $\sigma_{ij} = a\sigma'_{ij}$ from equation 14 and some algebraic manipulation, equation A-3 can be rewritten as

$$p(a|\mathbf{d},\mathbf{m}) = \left(\prod_{i=1}^{N_f}\prod_{j=1}^{N_x}\frac{1}{\sigma'_{ij}\sqrt{2\pi}}\right)\left(\frac{1}{a^2}\right)^{\frac{N_xN_f}{2}} \times \exp\left(-\frac{1}{a^2}\sum_{i=1}^{N_f}\sum_{j=1}^{N_x}\frac{(g_{ij}(\mathbf{m})-d_{ij})^2}{2\sigma_{ij}'^2}\right)p(a). \tag{A-4}$$

This equation can be rewritten as

$$p(a|\mathbf{d},\mathbf{m}) = L\tau^{\alpha-1}\exp(-\beta\tau), \tag{A-5}$$

where

$$\tau = \frac{1}{a^2}, \alpha = \frac{N_x N_f}{2} + 1, \beta = \sum_{i=1}^{N_f} \sum_{j=1}^{N_x} \frac{(g_{ij}(\mathbf{m}) - d_{ij})^2}{2\sigma_{ij}'^2}, \text{ and}$$

$$L = p(a)\left(\prod_{i=1}^{N_f} \prod_{j=1}^{N_x} \frac{1}{\sqrt{2\pi}\sigma_{ij}'}\right). \quad \text{(A-6)}$$

Assuming an (uninformative) uniform prior to the noise hyperparameter, $p(a)$ is a constant. Therefore, $L$ in equation A-5 also is independent of $a$. By having the exact formulation for the conditional posterior distribution of the noise hyperparameter, $a = \sqrt{1/\tau}$, we can sample the parameter posterior using a Gibbs sampler.

The Gibbs sampler is a special case of the MH algorithm: instead of accepting/rejecting a sample that is drawn from a proposal probability distribution, the Gibbs sampler draws a sample from the conditional posterior distribution of the desired parameter, equation A-5 in our case. Because of this, the proposed sample is always accepted (Geman and Geman, 1984). This makes the Gibbs sampler an efficient sampling algorithm for the introduced noise hyperparameter. We draw samples of the noise hyperparameter $a$ using a Gibbs step after each iteration of the RJMCMC sampler. Equation A-5 has the form of a gamma distribution. The Gibbs sampler then becomes the generation of random samples from a gamma distribution with the parameters given in equation A-5.

## REFERENCES


Ajo-Franklin, J. B., S. Dou, N. J. Lindsey, I. Monga, C. Tracy, M. Robertson, V. Rodriguez Tribaldos, C. Ulrich, B. Freifeld, T. Daley, and X. Li, 2019, Distributed acoustic sensing using dark fiber for near-surface characterization and broadband seismic event detection: Scientific Reports, **9**, 1328, doi: 10.1038/s41598-018-36675-8.

Aki, K., and P. G. Richards, 2002, Quantitative seismology: University Science Books.

Andrieu, C., J. de Freitas, and A. Doucet, 1999, Robust full Bayesian methods for neural networks: Advances in Neural Information Processing Systems.

Bakku, S. K., 2015, Fracture characterization from seismic measurements in a borehole: PhD thesis, Massachusetts Institute of Technology.

Barone, I., J. Boaga, A. Carrera, A. Flores-Orozco, and G. Cassiani, 2021, Tackling lateral variability using surface waves: A tomography-like approach: Surveys in Geophysics, **42**, 317–338, doi: 10.1007/s10712-021-09631-x.

Bodin, T., and M. Sambridge, 2009, Seismic tomography with the reversible jump algorithm: Geophysical Journal International, **178**, 1411–1436, doi: 10.1111/j.1365-246X.2009.04226.x.

Bodin, T., M. Sambridge, N. Rawlinson, and P. Arroucau, 2012, Transdimensional tomography with unknown data noise: Geophysical Journal International, **189**, 1536–1556, doi: 10.1111/j.1365-246X.2012.05414.x.

Bohlen, T., D. De Nil, D. Köhn, and S. Jetschny, 2016, SOFI2D seismic modeling with finite differences: 2D-elastic and viscoelastic version: User guide: Karlsruhe Institute of Technology.

Bohlen, T., S. Kugler, G. Klein, and F. Theilen, 2004, 1.5 D inversion of lateral variation of Scholte-wave dispersion: Geophysics, **69**, 330–344, doi: 10.1190/1.1707052.

Boiero, D., and L. V. Socco, 2010, Retrieving lateral variations from surface wave dispersion curves: Geophysical Prospecting, **58**, 977–996, doi: 10.1111/j.1365-2478.2010.00877.x.

Bostick, F., III, 2000, Field experimental results of three-component fiber-optic seismic sensors: 70th Annual International Meeting, SEG, Expanded Abstracts, 21–24, doi: 10.1190/1.1815889.

Buchen, P., and R. Ben-Hador, 1996, Free-mode surface-wave computations: Geophysical Journal International, **124**, 869–887, doi: 10.1111/j.1365-246X.1996.tb05642.x.

Daley, T. M., B. M. Freifeld, J. Ajo-Franklin, S. Dou, R. Pevzner, V. Shulakova, S. Kashikar, D. E. Miller, J. Goetz, J. Henninges, and S. Lueth, 2013, Field testing of fiberoptic distributed acoustic sensing (DAS) for subsurface seismic monitoring: The Leading Edge, **32**, 699–706, doi: 10.1190/tle32060699.1.

Dettmer, J., S. Molnar, G. Steininger, S. E. Dosso, and J. F. Cassidy, 2012, Transdimensional inversion of microtremor array dispersion data with hierarchical autoregressive error models: Geophysical Journal International, **188**, 719–734, doi: 10.1111/j.1365-246X.2011.05302.x.

Dosso, S. E., J. Dettmer, G. Steininger, and C. W. Holland, 2014, Efficient transdimensional Bayesian inversion for geoacoustic profile estimation: Inverse Problems, **30**, 114018, doi: 10.1088/0266-5611/30/11/114018.

Gelman, A., J. B. Carlin, H. S. Stern, and D. B. Rubin, 2014, Bayesian data analysis, 3rd ed.: Electronic Edition.

Geman, S., and D. Geman, 1984, Stochastic relaxation, Gibbs distributions, and the Bayesian restoration of images: IEEE Transactions on Pattern Analysis and Machine Intelligence, **PAMI-6**, 721–741, doi: 10.1109/TPAMI.1984.4767596.

Ghalenoei, E., J. Dettmer, M. Y. Ali, and J. W. Kim, 2022, Trans-dimensional gravity and magnetic joint inversion for 3-D earth models: Geophysical Journal International, **230**, 363–376, doi: 10.1093/gji/ggac083.

Gilks, W. R., S. Richardson, and D. Spiegelhalter, 1995, Markov chain Monte Carlo in practice: CRC Press.

Green, P. J., 1995, Reversible jump Markov chain Monte Carlo computation and Bayesian model determination: Biometrika, **82**, 711–732, doi: 10.1093/biomet/82.4.711.

Hasani, M. A., and G. Drijkoningen, 2023, Experiences with distributed acoustic sensing using both straight and helically wound fibers in surface-deployed cables — A case history in Groningen, The Netherlands: Geophysics, **88**, no. 6, B369–B380, doi: 10.1190/geo2022-0769.1.

Hayashi, K., and H. Suzuki, 2004, CMP cross-correlation analysis of multichannel surface-wave data: Exploration Geophysics, **35**, 7–13, doi: 10.1071/EG04007.

Johannessen, K., B. Drakeley, and M. Farhadiroushan, 2012, Distributed acoustic sensing — A new way of listening to your well/reservoir: Intelligent Energy International, SPE.

Kruiver, P. P., E. van Dedem, R. Romijn, G. de Lange, M. Korff, J. Stafleu, J. L. Gunnink, A. Rodriguez-Marek, J. J. Bommer, J. van Elk, and D. Doornhof, 2017, An integrated shear-wave velocity model for the Groningen gas field, The Netherlands: Bulletin of Earthquake Engineering, **15**, 3555–3580, doi: 10.1007/s10518-017-0105-y.

Lindsey, N. J., E. R. Martin, D. S. Dreger, B. Freifeld, S. Cole, S. R. James, B. L. Biondi, and J. B. Ajo-Franklin, 2017, Fiber-optic network observations of earthquake wavefields: Geophysical Research Letters, **44**, 11–792, doi: 10.1002/2017GL075722.

Luo, Y., J. Xia, J. Liu, Y. Xu, and Q. Liu, 2008, Generation of a pseudo-2D shearwave velocity section by inversion of a series of 1D dispersion curves: Journal of Applied Geophysics, **64**, 115–124, doi: 10.1016/j.jappgeo.2008.01.003.

Mata Flores, D., A. Sladen, J.-P. Ampuero, E. D. Mercerat, and D. Rivet, 2023, Monitoring deep sea currents with seafloor distributed acoustic sensing: Earth and Space Science, **10**, e2022EA002723, doi: 10.1029/2022EA002723.

Molenaar, M. M., D. J. Hill, P. Webster, E. Fidan, and B. Birch, 2012, First downhole application of distributed acoustic sensing for hydraulic-fracturing monitoring and diagnostics: SPE Drilling & Completion, **27**, 32–38, doi: 10.2118/140561-PA.

Nayak, A.J. Ajo-Franklin, and Imperial Valley Dark Fiber Team, 2021, Measurement of surface-wave phase-velocity dispersion on mixed inertial seismometer-distributed acoustic sensing seismic noise cross-correlations: Bulletin of the Seismological Society of America, **111**, 3432, doi: 10.1785/0120210028.

Neducza, B., 2007, Stacking of surface waves: Geophysics, **72**, no. 2, V51–V58, doi: 10.1190/1.2431635.

Noorlandt, R., G. Drijkoningen, J. Dams, and R. Jenneskens, 2015, A seismic vertical vibrator driven by linear synchronous motors: Geophysics, **80**, no. 2, EN57–EN67, doi: 10.1190/geo2014-0295.1.

Park, C. B., R. D. Miller, and J. Xia, 1999, Multichannel analysis of surface waves: Geophysics, **64**, 800–808, doi: 10.1190/1.1444590.

Paulsson, B., J. Fairborn, R. Goldman, B. Bunn, and D. Frederick, 1997, An all fiber optic borehole hydrophone array: 67th Annual International Meeting, SEG, Expanded Abstracts, 250–253, doi: 10.1190/1.1885876.

Qu, L., J. Dettmer, K. Hall, K. A. Innanen, M. Macquet, and D. C. Lawton, 2023, Trans-dimensional inversion of multimode seismic surface wave data from a trenched distributed acoustic sensing survey: Geophysical Journal International, **234**,1051–1062, doi: 10.1093/gji/ggad112.

Rahimi Dalkhani, A., T. Áustsdóttir, E. Gudnason, G. P. Hersir, X. Zhang, and C. Weemstra, 2024, Transdimensional ambient-noise surface wave tomography of the Reykjanes Peninsula, SW Iceland: Geophysical Journal International, **236**, 621–643, doi: 10.1093/gji/ggad435.

Rahimi Dalkhani, A., X. Zhang, and C. Weemstra, 2021, On the potential of 3D transdimensional surface wave tomography for geothermal prospecting of the Reykjanes Peninsula: Remote Sensing, **13**, 4929, doi: 10.3390/rs13234929.

Sambridge, M., 1999, Geophysical inversion with a neighbourhood algorithm — I. searching a parameter space: Geophysical Journal International, **138**, 479–494, doi: 10.1046/j.1365-246X.1999.00876.x.

Sambridge, M., 2014, A parallel tempering algorithm for probabilistic sampling and multimodal optimization: Geophysical Journal International, **196**, 357–374, doi: 10.1093/gji/ggt342.
Schaefer, J. F., L. Boschi, and E. Kissling, 2011, Adaptively parametrized surface wave tomography: Methodology and a new model of the European upper mantle: Geophysical Journal International, **186**, 1431–1453, doi: 10.1111/j.1365-246X.2011.05135.x.
Sen, M. K., and R. Biswas, 2017, Transdimensional seismic inversion using the reversible jump Hamiltonian Monte Carlo algorithm: Geophysics, **82**, no. 3, R119–R134, doi: 10.1190/geo2016-0010.1.
Socco, L. V., D. Boiero, S. Foti, and R. Wisén, 2009, Laterally constrained inversion of ground roll from seismic reflection records: Geophysics, **74**, no. 6, G35–G45, doi: 10.1190/1.3223636.
Socco, L. V., S. Foti, and D. Boiero, 2010, Surface-wave analysis for building near-surface velocity models — Established approaches and new perspectives: Geophysics, **75**, no. 5, 75A83–75A102, doi: 10.1190/1.3479491.
Strobbia, C., and S. Foti, 2006, Multi-offset phase analysis of surface wave data (MOPA): Journal of Applied Geophysics, **59**, 300–313, doi: 10.1016/j.jappgeo.2005.10.009.
Tarantola, A., 2005, Inverse problem theory and methods for model parameter estimation: SIAM.
Vantassel, J. P., B. R. Cox, P. G. Hubbard, and M. Yust, 2022, Extracting high-resolution, multi-mode surface wave dispersion data from distributed acoustic sensing measurements using the multichannel analysis of surface waves: Journal of Applied Geophysics, **205**, 104776, doi: 10.1016/j.jappgeo.2022.104776.
Vignoli, G., and G. Cassiani, 2010, Identification of lateral discontinuities via multioffset phase analysis of surface wave data: Geophysical Prospecting, **58**, 389–413, doi: 10.1111/j.1365-2478.2009.00838.x.
Vignoli, G., I. Gervasio, G. Brancatelli, J. Boaga, B. Della Vedova, and G. Cassiani, 2016, Frequency-dependent multi-offset phase analysis of surface waves: An example of high-resolution characterization of a Riparian Aquifer: Geophysical Prospecting, **64**, 102–111, doi: 10.1111/1365-2478.12256.
Vignoli, G., C. Strobbia, G. Cassiani, and P. Vermeer, 2011, Statistical multi-offset phase analysis for surface-wave processing in laterally varying media: Geophysics, **76**, no. 2, U1–U11, doi: 10.1190/1.3542076.
Wang, Y., 2016, Seismic inversion: Theory and applications: John Wiley & Sons.
Wathelet, M., 2008, An improved neighborhood algorithm: Parameter conditions and dynamic scaling: Geophysical Research Letters, **35**, L09301, doi: 10.1029/2008GL033256.
Weemstra, C., J. I. De Laat, A. Verdel, and P. Smets, 2021, Systematic recovery of instrumental timing and phase errors using interferometric surface-waves retrieved from large-N seismic arrays: Geophysical Journal International, **224**, 1028–1055, doi: 10.1093/gji/ggaa504.
Wielandt, E., 1993, Propagation and structural interpretation of non-plane waves: Geophysical Journal International, **113**, 45–53, doi: 10.1111/j.1365-246X.1993.tb02527.x.
Wu, D., X. Wang, Q. Su, and T. Zhang, 2019, A matlab package for calculating partial derivatives of surface-wave dispersion curves by a reduced delta matrix method: Applied Sciences, **9**, 5214, doi: 10.3390/app9235214.
Xia, J., R. D. Miller, and C. B. Park, 1999, Estimation of near-surface shear-wave velocity by inversion of Rayleigh waves: Geophysics, **64**, 691–700, doi: 10.1190/1.1444578.
Xiang, E., R. Guo, S. E. Dosso, J. Liu, H. Dong, and Z. Ren, 2018, Efficient hierarchical trans-dimensional Bayesian inversion of magnetotelluric data: Geophysical Journal International, **213**, 1751–1767, doi: 10.1093/gji/ggy071.
Yao, H., Z. Ren, J. Tang, R. Guo, and J. Yan, 2023, Trans-dimensional Bayesian joint inversion of magnetotelluric and geomagnetic depth sounding responses to constrain mantle electrical discontinuities: Geophysical Journal International, **233**, 1821–1846, doi: 10.1093/gji/ggad029.
Yildirim, I., 2012, Bayesian inference: Gibbs sampling: Technical Note, University of Rochester.
Yust, M. B., B. R. Cox, J. P. Vantassel, P. G. Hubbard, C. Boehm, and L. Krischer, 2023, Near-surface 2D imaging via FWI of DAS data: An examination on the impacts of FWI starting model: Geosciences, **13**, 63, doi: 10.3390/geosciences13030063.
Zhang, X., F. Hansteen, A. Curtis, and S. De Ridder, 2020, 1-D, 2-D, and 3-D Monte Carlo ambient noise tomography using a dense passive seismic array installed on the North Sea seabed: Journal of Geophysical Research: Solid Earth, **125**, e2019JB018552, doi: 10.1029/2019JB018552.
Zulic, S., E. Sidenko, A. Yurikov, K. Tertyshnikov, A. Bona, and R. Pevzner, 2022, Comparison of amplitude measurements on borehole geophone and DAS data: Sensors, **22**, 9510, doi: 10.3390/s22239510.

Biographies and photographs of the authors are not available.